

Newton-Marchenko-Rose Imaging: Image reconstruction based on inverse scattering theory

Jyoti Behura[†], Kees Wapenaar[‡] & Roel Snieder[†]

[†]Center for Wave Phenomena, Colorado School of Mines, Golden, Colorado

[‡]Delft University of Technology, Netherlands

ABSTRACT

Using only surface reflection data and first-arrival information, we generate the incoming and outgoing wavefields at every image point in the subsurface. An imaging condition is applied to these incoming and outgoing wavefields directly to generate the image. Since the above algorithm is based on exact inverse scattering theory, the reconstructed wavefields are accurate and contain all multiply scattered energy in addition to the primary event. As corroborated by our synthetic examples, imaging of these multiply scattered energy helps illuminate the subsurface better. We also demonstrate that it is possible to perform illumination compensation using our imaging algorithm that results in improved imaging at large depths. Other advantages include targeted imaging, potential reduction in computational time, parallelizable algorithm, imaging of high frequencies at no additional cost, and inexpensive imaging in anisotropic media.

Introduction

Wapenaar *et al.* (2011) propose a methodology for reconstructing the 3D impulse response for any “virtual source” in the subsurface using surface reflection data and the direct arrivals from the “virtual source” to the receivers on the surface. Their proposal is the 3D extension of the 1D iterative algorithm of Rose (2002b,a) who shows that in layered media, it is possible to focus all the energy at a particular time (or depth if the velocity is known) by using a complicated source signature. In other words, the complicated source signature is the impulse response between the surface location and the depth at which the wave is focused.

It is imperative to briefly discuss the pioneering work of V. Marchenko, R.G. Newton, and J.H. Rose on inverse scattering theory (Prosser, 1969; Gopinath & Sondhi, 1971; Burridge, 1980; Bojarski, 1981; Newton, 1989) that is instrumental in the development of the methodology of Rose (2002b,a) and Wapenaar *et al.* (2011, 2012a) and the imaging algorithm presented here. In 1D scattering theory, Marchenko’s integral equation (Marchenko, 2011) determines the relation between the wavefield in the interior of a medium and the reflected impulse response. It was originally derived for spherically symmetric media (and therefore 1D) and used only reflected waves. Newton (1980, 1981, 1982) derived a similar relation that uses

all scattered waves (reflected and transmitted) in 2D and 3D media. In 1D, this relation is given by

$$u^{+sc}(t, e, x) = \sum_{e'=-1,1} R(t + e'x, -e', e) + \sum_{e'=-1,1} \int_{-\infty}^{\infty} R(\tau + e'x, -e', e) u^{+sc}(\tau, e', x) d\tau, \quad (1)$$

where t is time, e is the direction of wave propagation, x is the 1D space, u^{+sc} represents the scattered wavefield, and R is the impulse response function. The above relation is known as the Newton-Marchenko integral equation (Newton, 1980, 1981, 1982) that solves for the wavefield inside a medium using the far-field scattered data. Newton used the 3D version of equation 1 to solve the inverse scattering problem for the Schrödinger wave equation. Rose *et al.* (1985) generalized the Newton-Marchenko equation to the scalar wave equation and also derived the equation for attenuative and time-dependent media (Rose *et al.*, 1986). Later, Budreck & Rose (1992) derived the relation for waves propagating in non-attenuative elastic media. A physical explanation of the above inverse scattering theory was provided by Rose (2002b,a) who showed that the ideas of focusing and time-reversal in fact result in the Newton-Marchenko equation.

The first step involved in solving for the scattering potential is to solve the Newton-Marchenko inte-

gral equation and find the wavefield everywhere inside the medium. Newton (1980, 1981, 1982) solved the inverse scattering problem for the Schrödinger wave equation by combining the Newton-Marchenko integral equation with high-frequency asymptotics. This approach becomes more complicated for the wave equation (Budreck & Rose, 1992). A significant breakthrough was made by Rose (2002b,a) who proposed an iterative approach, which he named ‘single-sided’ auto-focusing, that determines the wavefield in 1D media by focusing the incident wave at a specified time. Rose proved that the incident wave that focuses the wavefield in the interior comprises of a delta function (band-limited in practice) followed by the time-reversed solution of the Marchenko equation. Rose’s algorithm was recently implemented on 1D seismic data by Brogini *et al.* (2011) who again show that a ‘virtual source’ response can be generated from surface reflection data alone. Besides extending Rose’s iterative algorithm to higher dimensions, Wapenaar *et al.* (2011, 2012a) also showed that the wavefield at any interior location can also be decomposed into the “down-going” and “up-going” wavefields at the “virtual source”. They also proposed an algorithm to image internal multiples by generating virtual-source responses at various depth levels.

The “down-going” and “up-going” wavefields are in fact the incoming and outgoing wavefields, respectively, at the point of focus. Here, we show how the incoming and outgoing wavefields can be directly used for imaging the subsurface. In honor of the contribution of Newton, Marchenko, and Rose, we call the imaging algorithm introduced here as Newton-Marchenko-Rose Imaging, NMRI* in short. Besides demonstrating our imaging technique on synthetic examples, we discuss its advantages over existing imaging methods, in particular reverse-time migration (RTM).

1 ALGORITHM

Any seismic imaging algorithm consists of two steps - wavefield reconstruction and imaging condition. For example, RTM is a two-way imaging technique that utilizes wavefields reconstructed in time by accurately implementing the wave equation (Baysal *et al.*, 1983; Whitmore, 1983; McMechan, 1983) in a background velocity model. Under this technique, the source- and receiver-wavefields are reconstructed by forward-propagating the source signature and back-propagating the receiver recordings using a numerical solution of the wave equation (commonly a finite-difference algorithm). Wavefield reconstruction in RTM is followed by the application of an imaging condition (commonly cross-correlation) to image the reflectors. In other words, we

*NMRI also stands for Nuclear Magnetic Resonance Imaging which is a medical imaging technique.

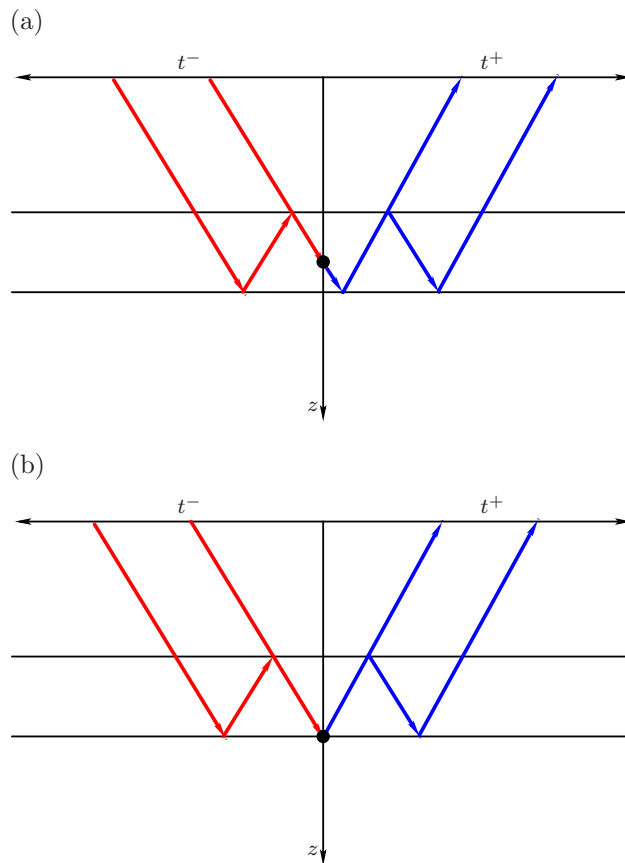


Figure 1. Schematic in 1D showing the anti-causal (G^- , incoming) and causal (G^+ , outgoing) Green’s functions, in red and blue respectively, for an image point (a) not on a reflector and (b) on a reflector. The black dot represents the point of focus where the incoming waves collapse and from where the outgoing waves are emitted.

find the similarity between the wavefield that is incident on the reflector and the wavefield that is reflected. The similarity will be high at the reflector position and low elsewhere. Imaging using RTM, however, assumes that all multiples (surface-related and internal) have been suppressed from the data; if not, the multiples could result in spurious events on the image.

NMRI, on the other hand, decomposes the wavefield into causal (G^+) and anti-causal (G^-) Green’s functions. G^+ and G^- make up the full Green’s function G which is the impulse response on the surface for a source at the image point. The causal Green’s function G^+ can be interpreted as the impulse response due to a source that is emitting such that the waves are outgoing from it (Figure 1a); while the anti-causal Green’s function G^- is due to an absorbing source such that the incoming waves collapse (or focus) onto the source location (Figure 1a) at a particular time.

In NMRI, as the incoming incident wavefield fo-

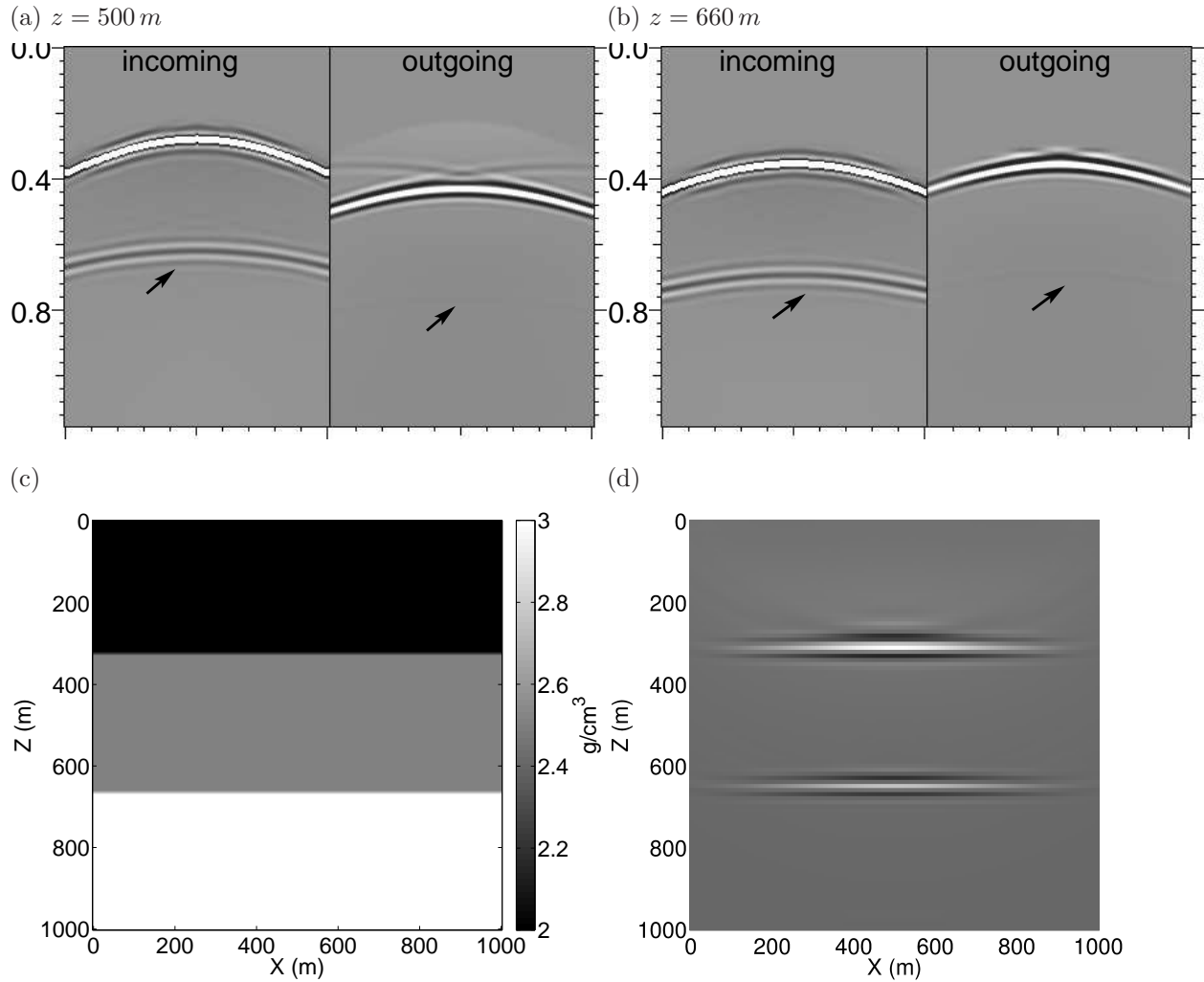


Figure 2. Incoming and outgoing wavefields at a reflector position (a) and a depth devoid of reflectors (b). The arrows point to parts of the wavefield generated from internal multiples. (c) The density model of the subsurface and (d) the NMRI image. A constant velocity of 2000 m/s was used for modeling and imaging. Since the normal-incidence reflection coefficient is approximately 0.1 for both reflectors, the internal multiples are weak.

causes at the imaging point, a reflection is generated depending on whether there is actually a reflector at that point in space (Figure 1). In the presence of a reflector (Figure 1b), the incident wavefield generates a reflected outgoing-wave, i.e. G^- and G^+ coincide kinematically. On the other hand, in the absence of a reflector at the image point (Figure 1a), no reflected waves are generated at the image point and $G^- \neq G^+$ kinematically. Therefore, only at a reflector location, the incoming-wavefield (G^-) coincides with the outgoing-wavefield (G^+) which gives rise to a non-zero zero-lag cross-correlation. The synthetic example in Figures 2a and 2b demonstrate the above arguments. For the image point at $z = 500\text{ m}$, the incoming and outgoing wave-

fields do not coincide (Figure 2a) while for $z = 660\text{ m}$, they do (Figure 2b).

Since the Newton-Marchenko equation is based on exact inverse scattering, the reconstructed incoming and outgoing wavefields contain all multiply-scattered energy. Therefore, the wavefields that are incident on and reflected from the scatterers contain all the multiply-scattered energy in addition to the direct transmitted arrival. Note the presence of these multiples in Figures 2a and 2b. Any multiply-scattered wave that is incident on a scatterer will also have a corresponding scattered wave occurring at the same time. In Figure 2b, the multiply-scattered incoming and outgoing waves coincide in time, while in Figures 2a, they do

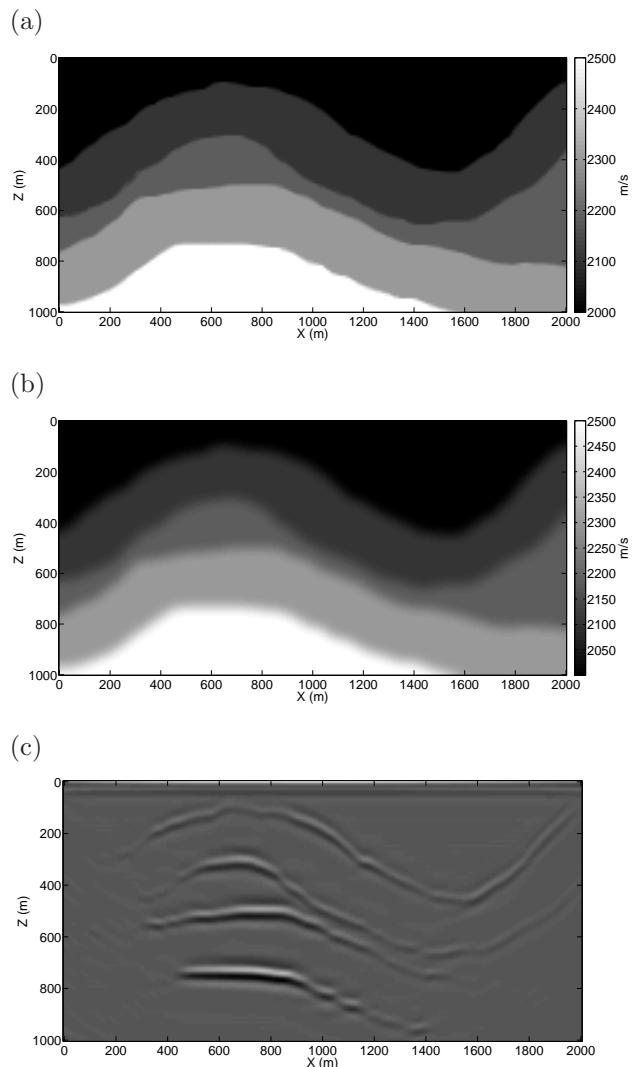


Figure 3. (a) The original velocity model of the fold system and (b) the smoothed version used for imaging and (c) the corresponding NMRI image. A constant density of 1 gm/cm^3 was used in generating the reflection data.

not. Hence, in addition to the primary wavefield, all multiply-scattered energy will also be imaged accurately using NMRI. Other advantages of NMRI are discussed later.

The pseudo-code for NMRI is given in Algorithm 1. The incoming and outgoing wavefields are constructed at every location in space using the recipe of Rose (2002b,a); Wapenaar *et al.* (2011). An imaging condition is applied to these two wavefields to obtain the image. Note that a background velocity model is necessary to compute the first arrivals at the surface from an impulse at the image point.

Algorithm 1 The NMRI algorithm. Superscript “ $-t$ ” represents time reversal and “ $*$ ” depicts convolution. u^{i0} are the first arrivals from the image point onto the surface, $u_{1,2}^i$ are the two types of incident waves and $u_{1,2}^r$ are the corresponding reflected wavefields at the surface, and R is the reflection response. G^+ and G^- are the causal (outgoing waves) and anti-causal (incoming waves) Green’s functions, respectively.

```

for any x,y,z in image space do
  Compute first arrivals  $u^{i0}$ 
  Initialize:
     $u_{1,2}^i \leftarrow u^{i0,-t}$ 
     $u_{1,2}^r \leftarrow 0$ 
  repeat
    Mute  $u_{1,2}^r$  beyond first arrivals
    Update incident wavefield:
       $u_1^i \leftarrow u^{i0} - u_{1,2}^{r,-t}$ 
       $u_2^i \leftarrow u^{i0} + u_{2,2}^{r,-t}$ 
    Update reflected wavefield:
       $u_1^r \leftarrow u_1^i * R$ 
       $u_2^r \leftarrow u_2^i * R$ 
  until  $u_{1,2}^r$  converge
   $G^+ + G^- = u_1^r + u_{1,2}^{i,-t}$ 
   $G^+ - G^- = u_2^r - u_{2,2}^{i,-t}$ 
  Solve for  $G^+$  and  $G^-$ 
  Imaging condition on  $G^+$  and  $G^-$ 
end for

```

2 NMRI IN ACTION

Here, we present three synthetic data results to demonstrate the performance and effectiveness of NMRI. The layer-cake (Figure 2) and Lena (Figure 4) models are constant velocity, variable density models while the fold model (Figure 3) has a variable velocity and constant density. The data acquisition is a fixed surface spread in each case where the sources and receivers are at $z = 0m$. The source and receiver spacing is $10m$ in all the three acquisitions. Time sampling is also the same ($0.004s$) in each case. The direct arrivals were muted from the shot gathers. Besides this, no other processing was performed on the data; the data contain all orders of internal multiples.

Ray-tracing was used in computing the first breaks for the layercake model and for Lena; for the fold model, the first breaks were computed using a finite-difference wave-propagation code in a smoothed version (Figure 3b) of the true velocity model. An incorrect background velocity model will result in incorrect positioning of the reflectors. Although not analyzed here, it would be interesting to study how the NMRI image would differ from the RTM image for an incorrect velocity model.

Note that NMRI produced a satisfactory image (Figures 2d,3c, 5a, and 5b) in each case. Some steeply-dipping events were not imaged accurately for the fold model and for Lena because of the lack of illumination of

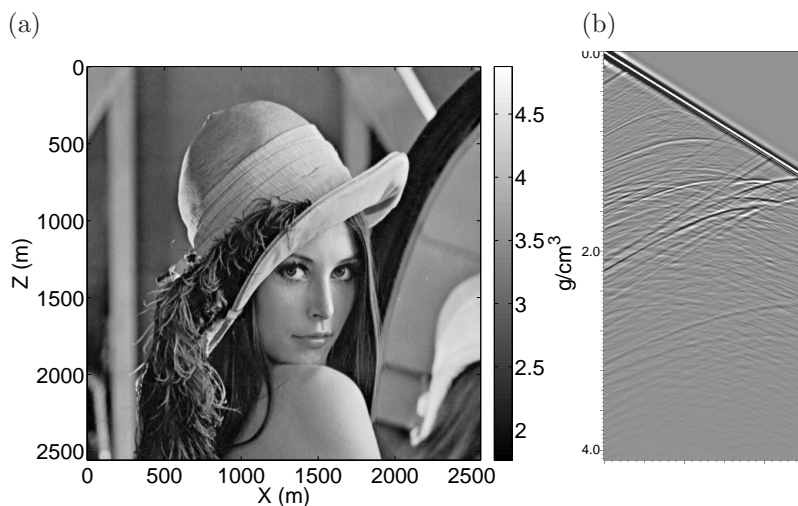


Figure 4. (a) The density model used in imaging Lena. (b) A sample shot gather. A constant velocity of 2000 m/s was used for modeling and imaging.

these features. Even though the reflection data is complicated (Figure 4b) and contains all orders of internal multiples, NMRI imaged the primary as well as all the scattered events appropriately.

3 ADVANTAGES OVER RTM

True amplitude/AVA: NMRI is based on exact inverse scattering theory and therefore the reconstructed wavefield in the interior of the medium is accurate irrespective of the velocity and density distributions in the subsurface. Hence, the NMRI image should be closer to the true reflectivity of the subsurface. Angle gathers for NMRI can be generated in the same way as in RTM. Amplitude variation with angle (AVA) analysis (on angle gathers) for NMRI, however, should be more reliable because the wavefields are accurate. Note that the amplitude of the first arrivals, however, might not be accurate because it is constructed from the best known background velocity and density models. Incorrect amplitude of the first arrivals would result in inaccurate amplitudes of the scattered waves.

Multiples are imaged: As mentioned above, since the wavefields in NMRI are reconstructed accurately, the image should be better than existing imaging algorithms. Also, all orders of multiples are reconstructed and imaged accurately. Reflectors not illuminated by the direct arrival, might be illuminated by internal multiples (Fleury, 2012); these reflectors would be visible on the NMRI image but not on the RTM image. Figure 5a is generated using only primaries while figure 5b results from imaging both primaries and internal multiples, with the difference between the two shown in figure 5c.

Since Figure 5a is generated using the correct Green's function (as the first arrival), it can be interpreted as the best possible RTM image (generated from data containing only primary reflections). Albeit marginally, internal multiples have contributed to the image at many locations (Figure 5c). Note that the internal multiples do not result in any random or spurious events in the image. This is also corroborated by the virtual-source imaging of internal multiples of Wapenaar *et al.* (2011) and Wapenaar *et al.* (2012b) who note that the image corresponds to the reflectivity of the model. Imaging of multiples also renders multiple (both surface-related and inter-bed) prediction and suppression unnecessary. Although, none of the examples presented here contain surface-related multiples, the theory underlying NMRI imposes no limitations on the type of multiples.

Illumination compensation: Illumination compensation can be performed by manipulating the amplitude of the leading delta function in the incident wavefield such that each primary arrival at the image point has the same amplitude. By using the same unit delta function for all first arrivals, we ensure that the reflector is equally illuminated from all incidence angles and has the same illumination at all depths. However, if the Green's function is used instead of a uniform delta function, the image at larger depths is poor because of insufficient illumination. Note that the above illumination compensation approach not only accounts for geometrical spreading but also for uneven and partial illumination at any image point. The image of Lena after illumination compensation is shown in Figure 5d. Clearly the NMRI image with illumination compensation (Figure 5d) is significantly better than the one without any compensation (Figure 5b). Application of a low-cut filter to Lena (Fig-

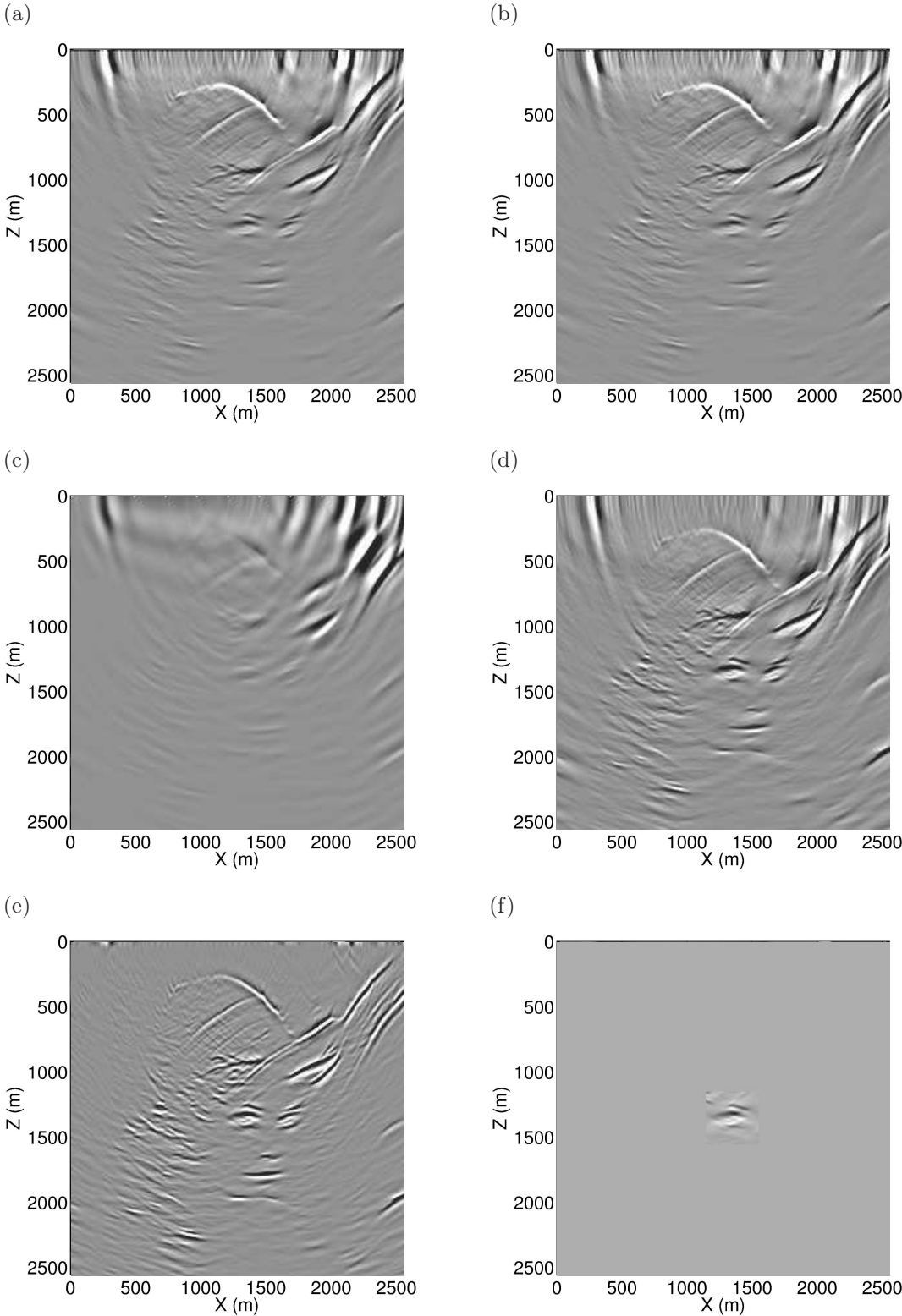


Figure 5. The NMRI image after one (a) and two (b) iterations and their difference (c). In (a) and (b), the Green's function is used for the first arrival. (d) The NMRI image after two iterations with illumination compensation, i.e. the same magnitude of delta function is used for all first arrivals. (e) Low-cut filtered version of (d). (f) Targeted imaging of Lena's left eye.

ure 5e) shows that many small details have been imaged in detail. Moreover, AVA would become more reliable as all the incident waves have the same amplitude. However, the effect of using a delta function instead of the Green's function on focusing and on the amplitudes of multiply scattered waves needs more thorough analysis. Irrespective of the illumination, some portions of image that have no reflected energy reaching the surface will never be imaged.

Targeted imaging: Note that for the computation of the image at any location in the image space, we need the first breaks at the surface for an impulse at the image point. Since the computation of the first breaks (using ray-tracing or finite-differences) can be done independently for each image point, it is possible to perform targeted imaging using NMRI. The targeted imaging of Lena's left eye is shown in Figure 5f. Wapenaar *et al.* (2011) also show that targeted imaging of internal multiples is possible using virtual-source wavefields.

Computationally cheap: The most expensive component of any imaging algorithm is the computation of the wavefield in the interior of the medium. In RTM, the source- and receiver-wavefields are computed by solving the wave equation numerically which makes the method expensive. In NMRI, wavefield computation is done through an iterative process which is computationally inexpensive. For each image point, only a single run of ray-tracing is necessary to compute the first arrivals which are used for an initial guess of the incident wavefield. Thereafter, both the reflected and incident-wavefields are updated using the iterative procedure described in Algorithm 1 (in our tests two iterations were enough in most cases). The updated scattered field is obtained by convolving the updated incident wavefield with the reflected impulse response (recorded data) for each iteration. The low computational cost of ray-tracing (or Gaussian-beam modeling) and a set of convolutions can make NMRI significantly faster than RTM. For complicated subsurfaces, however, an accurate first-arrival might be necessary which would necessitate the use of a finite-difference approach for its computation. In this case, NMRI does not hold any computational advantage over RTM. Other solutions like Gaussian-beam modeling may be adopted to alleviate this problem.

High frequencies: The cost of RTM increases significantly with increasing frequency content because the extrapolation grid has to be more finely sampled. Wavefield computation using NMRI, on the other hand, has no such limitation because the frequency content of the incident wave and the impulse response are only limited by the temporal Nyquist limit.

Highly parallelizable: Since the image at each location in the image space can be computed independently, the algorithm is highly parallelizable in the image space. For example, if there are 100 grid points in the image space, 100 processes could be run simultaneously on a cluster to obtain the image.

Anisotropy: Wavefield extrapolation in anisotropic media using numerical methods is expensive. In addition, depending on the dispersion relation used, the wavefield can contain shear-wave artifacts and incorrect P-wave amplitudes. In NMRI, however, if the first breaks are computed using ray-tracing, then imaging in anisotropic media becomes extremely cheap compared to RTM. Moreover, the wavefields in NMRI are accurate in amplitude even if the medium exhibits velocity anisotropy.

4 DISCUSSION AND CONCLUSIONS

The first arrivals at the surface from an impulse at any image point can be computed either using ray-tracing or solving the wave equation numerically using finite-differences. If the true phase and amplitude of the first arrival is desired, one can use dynamic ray-tracing or Gaussian-beam modeling. However, to produce an image with illumination compensation, it is enough to do kinematic ray-tracing followed by a convolution with a delta function (Rose, 2002b,a). If the background velocity field results in multipathing, one must make sure that the incident wavefield contains all multiple arrivals; if not, the incident wave would not produce a quality focus at the image point.

Wapenaar *et al.* (2012a) also demonstrate that the phase of the direct arrival is important in obtaining the correct amplitude and phase of the retrieved impulse response. To achieve this one can generate the first arrivals by numerically solving the wave-equation. In order to compensate for illumination, one must normalize each incident wave with its energy content to make sure that all incident waves have similar energy. As shown above, in the absence of normalization, deeper reflectors will not be illuminated adequately.

For a relatively uncomplicated subsurface, ray-tracing should suffice; the numerical solution of wave equation might be necessary for intricate first arrivals. Ray-tracing, however, has one significant advantage: it is substantially cheaper than solving the wave equation numerically (especially in anisotropic media). If minimizing computational cost is desired, ray-tracing should be the preferred method for computing the first arrivals.

Implementation of NMRI requires the construction of special shot-point gathers, which we call common surface-point gathers. Here, each bin location in the survey is a shot-point and every other bin is a receiver. Besides using conventional shot gathers in their construction, reciprocity can be used to further populate the common surface-point gathers. If no real traces exist for the shot and receiver combination, the trace can be interpolated or just assigned a null value. To reduce computational cost, an aperture can also be defined as done in many existing imaging algorithms.

Newton-Marchenko-Rose Imaging, which is based on exact inverse scattering theory, shows promise in

imaging complicated subsurfaces. Besides primaries, it can be used for illumination compensation and can image both surface-related and internal multiples. This should make NMRI useful for imaging poorly illuminated areas, especially underneath salt bodies. In comparison to RTM, NMRI has other important advantages, such as, it is potentially computationally cheaper, can image arbitrarily anisotropic media, can be used for targeted imaging, and should generate accurate AVA response.

ACKNOWLEDGMENTS

The implementation of NMRI was done using freeDDS. Discussions with Farnoush Forghani, Filippo Brogini, Clement Fleury, and Francesco Perrone were very useful. Support for this work was provided by the Consortium Project on Seismic Inverse Methods for Complex Structures at CWP.

References

- Baysal, E., Kosloff, D. D., & Sherwood, J. W. C. 1983. Reverse time migration. *Geophysics*, **48**(11), 1514–1524.
- Bojarski, N.N. 1981. Inverse scattering inverse source theory. *J. Math. Phys.*, **22**, 1647–1650.
- Brogini, F., Snieder, R., & Wapenaar, K. 2011. Connection of scattering principles: Focusing the wavefield without source or receiver. *SEG Technical Program Expanded Abstracts*, **30**(1), 3845–3850.
- Budreck, D. E., & Rose, J. H. 1992. A Newton–Marchenko equation and generalized optical theorem for elastodynamics. *Journal of Mathematical Physics*, **33**(8), 2903–2915.
- Burridge, R. 1980. The Gel'fand-Levitan, the Marchenko and the Gopinath-Sondi Integral Equations of Inverse Scattering Theory, Regarded in the Context of the Inverse Impulse Response Problems. *Wave Motion*, **2**, 305–323.
- Fleury, C. 2012. *Increasing illumination and sensitivity of reverse-time migration with internal multiples*. Tech. rept. CWP-716. Center for Wave Phenomena, Colorado School of Mines.
- Gopinath, B., & Sondhi, M.M. 1971. Inversion of the telegraph equation and the synthesis of nonuniform lines. *Proceedings of the IEEE*, **59**(3), 383 – 392.
- Marchenko, V. A. 2011. *Sturm-Liouville operators and applications*. 2 edn. Providence: American Mathematical Society.
- McMechan, G. A. 1983. Migration by extrapolation of time-dependent boundary values. *Geophysical Prospecting*, **31**(3), 413–420.
- Newton, R. G. 1980. Inverse scattering II. Three dimensions. *Journal of Mathematical Physics*, **21**(7), 1698–1715.
- Newton, R. G. 1981. Inverse scattering III. Three dimensions, continued. *Journal of Mathematical Physics*, **22**(10), 2191–2200.
- Newton, R. G. 1982. Inverse scattering IV. Three dimensions: generalized Marchenko construction with bound states, and generalized Gel'fand–Levitan equations. *Journal of Mathematical Physics*, **23**(4), 594–604.
- Newton, R.G. 1989. *Inverse Schrödinger Scattering in Three Dimensions*. Berlin: Springer Verlag.
- Prosser, R.T. 1969. Formal Solutions of Inverse Scattering Problems. *J. Math. Phys.*, **10**, 1819–1822.
- Rose, J. H. 2002a. *Time reversal, focusing and exact inverse scattering*. 1 edn. Springer-Verlag, Berlin. Pages 97–105.
- Rose, J. H. 2002b. Single-sided autofocusing of sound in layered materials. *Inverse Problems*, **18**, 19231934.
- Rose, J. H., Cheney, M., & DeFazio, B. 1985. Three-dimensional inverse scattering: Plasma and variable velocity wave equations. *Journal of Mathematical Physics*, **26**(11), 2803–2813.
- Rose, J. H., Cheney, M., & DeFazio, B. 1986. Determination of the Wave Field from Scattering Data. *Phys. Rev. Lett.*, **57**(Aug), 783–786.
- Wapenaar, K., Brogini, F., & Snieder, R. 2011. A proposal for model-independent 3D wave field reconstruction from reflection data. *SEG Technical Program Expanded Abstracts*, **30**(1), 3788–3792.
- Wapenaar, K., Brogini, F., & Snieder, R. 2012a. Creating a virtual source inside a medium from reflection data: a stationary-phase analysis. *Geophysical Journal International*, **189**, 001–006.
- Wapenaar, K., Thorbecke, J., van der Neut, J., Brogini, F., & Snieder, R. 2012b. Creating virtual sources inside an unknown medium from reflection data: a new approach to internal multiple elimination. *Page submitted of: Extended Abstracts*. European Association of Geoscientists and Engineers.
- Whitmore, N. D. 1983. Iterative depth migration by backward time propagation. *SEG Technical Program Expanded Abstracts*, **2**(1), 382–385.